



# Size Effect Analysis for the Characterization of Marcellus Shale Quasi-brittle Fracture Properties

Weixin Li<sup>1,2</sup> · Zhefei Jin<sup>2</sup> · Gianluca Cusatis<sup>1,2</sup>

Received: 24 August 2017 / Accepted: 12 August 2018 / Published online: 24 August 2018  
© Springer-Verlag GmbH Austria, part of Springer Nature 2018

## Abstract

The fracture characterization of shale rocks requires understanding the scaling of the measured properties to enable the extrapolation from small-scale laboratory tests to field applications. In this study, the fracture properties of Marcellus shale were obtained through size effect tests. Fracture tests were conducted on three-point-bending specimens with increasing size. The test results show that the nominal strength decreases with increasing specimen size and it can be fitted well by Bažant's size effect law. This demonstrates that shale fracture behavior deviates from classical linear elastic fracture mechanics (LEFM), and it has quasi-brittle characteristics. This implies, in turn, that the fracture toughness (or fracture energy) computed according to LEFM is size-dependent and, in general, cannot be considered a material property. Furthermore, the size effect analysis allows one to accurately identify the quasi-brittle fracture properties, namely the initial fracture energy and the effective fracture process zone length. A significant anisotropy was observed in the fracture properties determined with three principal notch orientations.

**Keywords** Marcellus shale · Size effect · Fracture energy · Fracture toughness · Fracture process zone · Quasi-brittle

## List of Symbols

$G$	Energy release rate	$D_0$	Transitional size
$G_{Ic}$	Effective LEFM fracture energy	$\hat{D}$	Normalized size
$G_f$	Initial fracture energy	$l_1$	Hillerborg's characteristic length
$G_F$	Total fracture energy	$L, D, t$	Specimen length, depth, and thickness
$K_{IcA}$	Apparent fracture toughness calculated using LEFM	$S$	Support span
$K_I$	Mode I stress intensity factor	$a$	Crack length
$K_{Ic}$	Fracture toughness	$a_0$	Notch length (equal to initial crack length)
$K_{IcA}$	Apparent fracture toughness calculated using LEFM	$\alpha$	Dimensionless crack length
$\ell_{FPZ}$	Length of FPZ	$\alpha_0$	Dimensionless notch length (equal to the initial value of $\alpha$ )
$c_f$	Effective FPZ length	$P$	Applied load
$\sigma(\delta)$	Cohesive stress as a function of crack opening $\delta$	$P_u$	Peak load
$f'_t$	Tensile strength of cohesive law	$\sigma_N$	Nominal stress
$\beta$	Brittleness number	$\sigma_{Nu}$	Nominal strength (nominal stress at peak load)
		$E, E'$	In-plane and out-of-plane modulus of material
		$\nu, \nu'$	In-plane and out-of-plane Poisson's ratio of material
		$G'$	Out-of-plane shear modulus of material
		$E_x, E_y$	Elastic constants (Young's modulus) in the specimen coordinate system
		$\nu_{xy}, \nu_{yx}$	Elastic constants (Poisson's ratio) in the specimen coordinate system
		$G_{xy}$	Elastic constants (shear modulus) in the specimen coordinate system
		$\lambda, \rho$	Dimensionless elastic constants

✉ Gianluca Cusatis  
g-cusatis@northwestern.edu

Weixin Li  
w.li@u.northwestern.edu

<sup>1</sup> Theoretical and Applied Mechanics, Northwestern University, Evanston, IL 60208, USA

<sup>2</sup> Department of Civil and Environmental Engineering, Northwestern University, Evanston, IL 60208, USA

$E^*$	Effective elastic modulus
$g, g'$	Dimensionless energy release rate and its derivative
$g_0, g'_0$	Dimensionless energy release rate at $\alpha_0$ and its derivative value
$k$	Dimensionless stress intensity factor
$\xi$	Dimensionless function
$\sigma_0$	A parameter in size effect law
$\text{MAPE}_{\alpha_0}$	Notch-machining error
$R^2$	Coefficient of determination
RMSE	Root-mean-squared error
SD	Standard deviation
SE	Standard error

## 1 Introduction

In recent years, the study of different aspects of shale rocks has surged as a result of the vital role that they play in various energy-related applications including oil and gas production, subsurface carbon dioxide sequestration, and nuclear waste disposal. Understanding the fundamental mechanical processes in shale formations, as well as their interaction with the in-situ stress field, pore pressure, and hydraulic loading, is essential to promote industrial innovations such as the development of the hydraulic fracturing techniques. In particular, of critical importance is the experimental and computational study of crack initiation and propagation as well as the identification of the fracture properties required to apply fracture mechanics theories and numerical simulation tools to field applications [see, e.g., Li et al. (2016, 2017, 2018b), Chau et al. (2016), Zeng et al. (2018), Zia et al. (2018)].

Fracture characterization of shale is usually based on linear elastic fracture mechanics (LEFM). The LEFM mode I fracture toughness has been used widely for the characterization of intact rock with respect to its resistance to crack propagation. Schmidt (1977) investigated the fracture toughness of Anvil Point oil shale using notched three-point-bending specimens with varying notch orientations with respect to the rock bedding. The measured fracture toughness values, varying from 0.3 to 1.1 MPa $\sqrt{\text{m}}$ , were found to decrease with an increase in kerogen content and were highest for notches orthogonal to the bedding and lowest for notches parallel to the bedding. Chong et al. (1987) proposed a semi-circular bend (SCB) specimen subjected to three-point-bending loading for fracture toughness measurements of Colorado oil shale. The obtained values for notches orthogonal to the bedding were determined using a stress intensity factor method, a compliance method, and a  $J$ -integral based method and were reported to vary from 0.88 to 1.0 MPa $\sqrt{\text{m}}$ . In contrast to Schmidt's observation (Schmidt 1977), it was

found that the static fracture toughness of organic-rich oil shale is higher than that of lean material.

By means of a similar test configuration, Sierra et al. (2010) reported the fracture toughness of Woodford shale to be in the range of 0.74–1.17 MPa $\sqrt{\text{m}}$  and to be related to the clay content of the samples. Lee et al. (2015) performed SCB tests on Marcellus shale core containing calcite-filled natural fractures (veins). These tests showed that the presence of calcite-filled veins has a significant effect on the crack propagation path. For the specimens without veins, the fracture toughness was reported to vary from 0.18 to 0.73 MPa $\sqrt{\text{m}}$  depending on the specimen bedding plane orientations. Chandler et al. (2016) reported fracture toughness measurements on Mancos shale using a modified short-rod methodology. The highest fracture toughness value, 0.72 MPa $\sqrt{\text{m}}$  was obtained for notches normal to the bedding, and the lowest one, 0.21 MPa $\sqrt{\text{m}}$  for notches aligned with the bedding. In addition to the conventional fracture tests, micro-scale scratch tests (Hubler and Ulm 2016; Akono and Kabir 2016; Kabir et al. 2017) were also utilized for the fracture characterization of various types of shale rocks.

In addition to the aforementioned dependence on the organic content of samples, several studies have shown that the laboratory-determined fracture characteristics of shale and shale-like rocks are influenced by the water content (Lim et al. 1994; Chen et al. 2017; Yan et al. 2017) and the loading rate (Kabir et al. 2017). Although important, these aspects are beyond the scope of the study presented in this paper in which only dry specimens and quasi-static loading conditions were considered.

Despite the abundance of shale fracture experimental data, only a few studies focused on the size and geometry dependence of shale fracture properties measured in laboratory tests. Wang et al. (2017) measured the fracture toughness of a shale outcrop in Chongqing, China, using SCB and cracked chevron notched Brazilian disk (CCNBD) specimens, and noticed that the obtained toughness values from these two methods were different.

The measured toughness of various geomaterials was observed to vary with the shape and size of the investigated specimens (Ingraffea et al. 1984; Kataoka and Obara 2015; Barpi et al. 2012; Bocca et al. 1989; Khan and Al-Shayea 2000; Wang and Hu 2017; Ayatollahi and Akbardoost 2014). For instance, Kataoka and Obara (2015) observed that the fracture toughness of Kimachi sandstone increased as the radius of the SCB specimens increases from 12.5 to 150 mm, and converged to a constant value for a radius larger than 70 mm.

Furthermore, it has been known for some time that laboratory measurements of LEFM fracture toughness underestimate the in-situ toughness determined from field data (Chong et al. 1989; Chong and Smith 1984).

The size and shape dependence of the LEFM fracture properties suggests that shale has a quasi-brittle fracture behavior characterized by a non-negligible size of the fracture process zone (FPZ) (Bažant 1984). The FPZ is a volume of material ahead of the crack tip in which (1) the material experiences damage and softening; (2) the stress field is nonuniform, and the magnitude of the stresses decreases with increasing deformation. This violates the LEFM assumption that the energy dissipation associated with fracture occurs in one mathematical point. Hence, nonlinear fracture mechanics approaches must be adopted for the correct analysis of fracture phenomena in quasi-brittle materials in general and shale rocks in particular.

## 2 Fracture Mechanics and Size Effect of Anisotropic Quasi-brittle Materials

This section reviews two fracture mechanics approaches, namely the equivalent linear elastic fracture mechanics and the cohesive crack model, which have been adopted extensively in the literature for the analysis of quasi-brittle fracture and, more specifically, for the interpretation of size effect tests on quasi-brittle materials. The discussion is limited to the case of orthotropic material symmetry, which includes the case of shale.

### 2.1 Equivalent Linear Elastic Fracture Mechanics

According to Bao et al. (1992), the Mode I stress intensity factor,  $K_I$ , of a specimen with crack length  $a$  subject to bending (see Fig. 1) and made of an orthotropic material can be written as follows:

$$K_I = \sigma_N \sqrt{D} k(\alpha, \rho, \psi) = \sigma_N \xi(\alpha, \rho, \psi) \sqrt{\pi D \alpha}, \tag{1}$$

where  $\sigma_N$  is the nominal stress,  $k(\alpha, \rho, \psi)$  and  $\xi(\alpha, \rho, \psi)$  are dimensionless functions,  $\alpha = a/D$  is the dimensionless crack length,  $D =$  specimen depth,  $\psi = \lambda^{1/4} S/D$ , and  $S =$  specimen span.  $\lambda = E_x/E_y$ ,  $\rho = 0.5(E_x E_y)^{1/2}/G_{xy} - (v_{xy} v_{yx})^{1/2}$  are dimensionless elastic constants and  $E_x, E_y, v_{xy}, v_{yx}, G_{xy}$  are

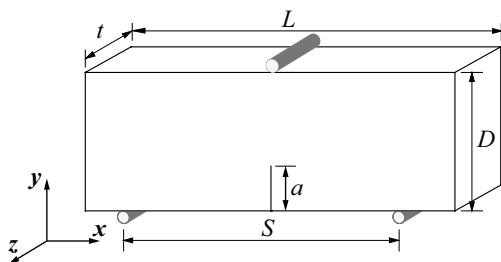


**Fig. 1** Geometry of the three-point-bending test setup, in which  $L, D$ , and  $t$  represent specimen length, depth, and thickness, respectively;  $S$  is the span;  $a$  is the crack length

the elastic constants defined in the Cartesian coordinate system depicted in Fig. 1. For a three-point-bending test, the nominal stress can be defined as follows:

$$\sigma_N = 1.5 \frac{S}{D} \frac{P}{Dt}, \tag{2}$$

where  $P =$  applied load and  $t =$  specimen thickness.

Furthermore, under plane stress conditions, the energy release rate,  $G$ , can be calculated as follows:

$$G = \frac{K_I^2}{E^*} = \frac{\sigma_N^2 D}{E^*} g(\alpha, \rho, \psi), \tag{3}$$

where

$$g(\alpha, \rho, \psi) = k(\alpha, \rho, \psi)^2 = \pi \alpha \xi(\alpha, \psi, \rho)^2 \tag{4}$$

and

$$E^* = \sqrt{\frac{2E_x E_y \lambda^{1/2}}{1 + \rho}}. \tag{5}$$

Equation (3) represents Irwin’s relation for orthotropic materials under plane stress and is similar to the one for isotropic materials except that the effective elastic modulus,  $E^*$ , is used as opposed to the isotropic modulus of elasticity. Equation (3) was first proposed by Sih et al. (1965) and has been adopted widely in the literature [see, e.g., (Bao et al. 1992; Bažant et al. 1996; Kim et al. 2013; Salviato et al. 2016b)], but its validity is limited to mode I fracture whose propagation is aligned with the axes of symmetry of the material. Indeed, Eq. (3) can be shown to be a particular case of the generalized formulation proposed by Laubie and Ulm (2014a, b), which accounts for generic fracture modes and fracture orientations.

On the basis of the equivalent LEFM, the peak load condition for “positive” specimen geometries (i.e., the ones characterized by  $g'(\alpha) > 0$ ) can be written (Bažant 1984; Bažant and Planas 1997) with reference to an equivalent crack length,  $a = a_0 + c_f$  ( $\alpha = \alpha_0 + c_f/D$ ), as:

$$G(\alpha_0 + c_f/D) = \frac{\sigma_{Nu}^2 D}{E^*} g(\alpha_0 + c_f/D) = G_{Ic}, \tag{6}$$

where  $\sigma_{Nu}$  is the nominal stress at the peak load (nominal strength),  $a_0$  is the notch length of the notched specimen that is equal to the initial crack length before fracture propagation occurs,  $\alpha_0 = a_0/D$  is the dimensionless notch length (equal to the initial value of the dimensionless crack length  $\alpha$ ),  $G_{Ic}$  and  $c_f$  are the effective LEFM fracture energy and the effective FPZ length, respectively, both assumed to be material properties. Note that the term notch is used interchangeably with the initial crack in this work consistently to the available LEFM literature, because the notches are assumed to be sharp (with zero radius of curvature at the tip). For

orthotropic materials,  $G_{Ic}$  and  $c_f$  have, in general, different values for different fracture orientations. The fracture energy can be related to the fracture toughness,  $K_{Ic}$ , through Irwin’s relation:  $G_{Ic} = K_{Ic}^2/E^*$ . In Eq. (6) and in what follows, the direct dependence of  $g(\cdot)$  on  $\psi$  and  $\rho$  is dropped for simplicity of notation.

The concept of effective FPZ is introduced to account for the non-negligible size of the actual FPZ, as illustrated in Fig. 2. It is worth pointing out that the FPZ is assumed to be fully developed at peak load, which means that the stress profile varies from zero at the notch tip to the tensile strength at the tip of the FPZ (see Fig. 2). In addition, (1) the length of fully developed FPZ length,  $\ell_{FPZ}$ , is assumed to be a material property and, as such, size-independent; (2)  $c_f$  is assumed to be proportional to  $\ell_{FPZ}$ , and the ratio  $c_f/\ell_{FPZ} \approx 0.5$  is often reported in the literature (Bažant and Planas 1997).

By approximating  $g(\alpha_0 + c_f/D)$  with only the linear term of its Taylor series expansion at  $\alpha_0$ , one obtains

$$\sigma_{Nu} = \sqrt{\frac{E^*G_{Ic}}{Dg_0 + c_f g'_0}}, \tag{7}$$

where  $g_0 = g(\alpha_0)$  and  $g'_0 = g'(\alpha_0)$  are size-independent only in the case of geometrically similar specimens, i.e., for  $\alpha = \text{constant}$  and  $\psi = \text{constant}$ .

Equation 7 is known as Bažant’s size effect law (SEL) and it can be also recast in the following form:

$$\sigma_{Nu} = \frac{\sigma_0}{\sqrt{1 + \beta}}, \tag{8}$$

where  $\sigma_0 = (E^*G_{Ic}/(c_f g'_0))^{1/2}$ ;  $\beta = D/D_0$ , also called brittleness number;  $D_0 = c_f g'_0/g_0$ . It is interesting to note that Eq. (8) incorporates a characteristic size  $D_0$  which is usually

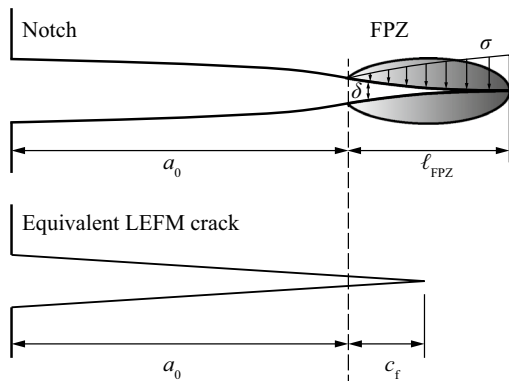


**Fig. 2** Fully developed fracture process zone (FPZ) and equivalent LEFM crack length at peak load.  $\sigma$  represents cohesive stress as a function of crack opening,  $\delta$ ;  $a_0$  is the notch length (equal to the initial crack length);  $\ell_{FPZ}$  represents the FPZ length;  $c_f$  represents the so-called effective FPZ length

called the transitional size and is the key to describe the transition from ductile to brittle behavior with increasing size.

### 2.2 Cohesive Crack Model

Another approach widely used to account for the finite size of the FPZ is the cohesive crack model pioneered by Dugdale (1960) and Barenblatt (1962) for ductile materials with the name “cohesive zone model” and by Hillerborg et al. (1976) for concrete with the name “fictitious crack model”. According to the cohesive crack model, the FPZ is simulated as a crack that is able to transfer stress across the crack plane. For a mode I fracture, the cohesive tractions are assumed to be orthogonal to the crack plane and to be governed by the so-called cohesive law,  $\sigma(\delta)$ , consisting of a decreasing function of the crack opening,  $\delta$ , as depicted in Fig. 3. Depending upon the material of interest, the cohesive crack law can be formulated with various functions. However, in most cases, such functions depend on three key parameters (see Fig. 3): the tensile strength,  $f'_t$ , characterizing crack initiation; the total fracture energy,  $G_F$ , defined as the area under the cohesive law; the initial fracture energy,  $G_f$ , defined as the area under the initial, almost linear portion of the cohesive law (see Fig. 3). The ratio  $G_F/G_f$  depends on the functional form describing the cohesive law: for example, for a linear function  $G_F/G_f = 1$  and for an exponential function  $G_F/G_f = 2$ .

For a linear cohesive law, the cohesive crack model predicts the nominal strength of notched specimens to be consistent with Bažant’s SEL (Eq. 7) for  $G_{Ic} = G_f = G_F$  and  $\hat{D} > 0.2$ , where  $\hat{D} = g_0 D / (g'_0 l_1)$  is normalized size, and  $l_1 = E^* G_f / f_t'^2$  is Hillerborg’s characteristic length (Hillerborg et al. 1976). Cedolin and Cusatis (2008) and Cusatis and Schaufert (2009) showed that the condition  $\hat{D} > 0.2$  ensures the cohesive stress at the notch tip to be close to zero and, consequently, the FPZ to be fully developed. Instead, in the case of a nonlinear cohesive law, Cusatis and Schaufert

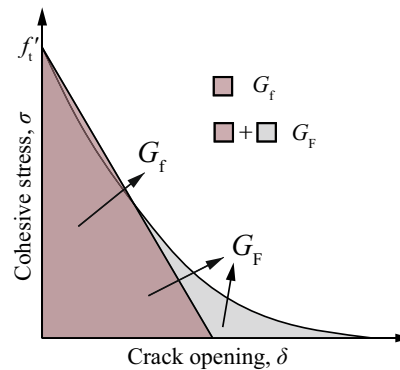


**Fig. 3** Typical cohesive crack law characterized by the tensile strength,  $f'_t$ ; the initial fracture energy,  $G_f$ ; total fracture energy,  $G_F$

(2009) showed that the predictions of the cohesive crack model agree with Eq. (7) for  $G_{Ic} = G_f$  and  $0.2 \leq \hat{D} \leq 2$  and for  $G_{Ic} = G_F$  and  $\hat{D} > 10$ . The former conditions correspond to cohesive stress values in the initial portion of the cohesive law, whereas the latter conditions correspond to a fully developed FPZ. Finally, still for a nonlinear cohesive law, the cohesive crack model and the effective LEFM predictions deviate significantly one from the other for  $2 \leq \hat{D} \leq 10$  (Cedolin and Cusatis 2008; Cusatis and Schaufert 2009). In this size range, the cohesive stresses are not within the initial portion of the cohesive law, and the FPZ is not fully developed.

Based on these results, Cusatis and Schaufert (2009) concluded that for typical laboratory size specimens, the FPZ cannot be fully developed at peak load and size effect tests cannot be used to identify  $G_F$  unless the material is characterized by a linear cohesive law. On the contrary, size effect results on typical laboratory specimens of certain sizes can be fitted by Eq. (7) to identify  $G_f$  regardless of the shape of the cohesive law. This is known in the literature as the “size effect method”, and it was proposed originally by Bažant for concrete (Bažant 1984; Bažant and Pfeiffer 1987; Bažant and Planas 1997).

Furthermore, for the size range in which the cohesive crack model and the equivalent LEFM with  $G_{Ic} = G_f$  provide similar results, Cusatis and Schaufert (2009) showed that  $c_f \approx 0.44l_1$ . Using this relationship, it is possible to estimate the tensile strength by means of size effect tests as  $f'_t = (0.44E^*G_f/c_f)^{1/2}$ .

The size effect method has been used by many authors for concrete and mortar (Bažant and Pfeiffer 1987; Bažant and Kazemi 1990a; Cedolin and Cusatis 2008), polymer composites (Bažant et al. 1996; Salviato et al. 2016b; Meford et al. 2017), ceramics (Bažant and Kazemi 1990b), wood (Aicher 2010), rocks such as limestone (Bažant et al. 1991) and granite (Bažant and Kazemi 1990a), and some biomaterials (Kim et al. 2013), just to mention a few. A similar approach was proposed by Akono (2016), Hubler

and Ulm (2016) for the interpretation of scratch tests at the nano- and micro-scale.

In the work presented in this paper, the size effect method was applied to the characterization of the fracture parameters of Marcellus shale.

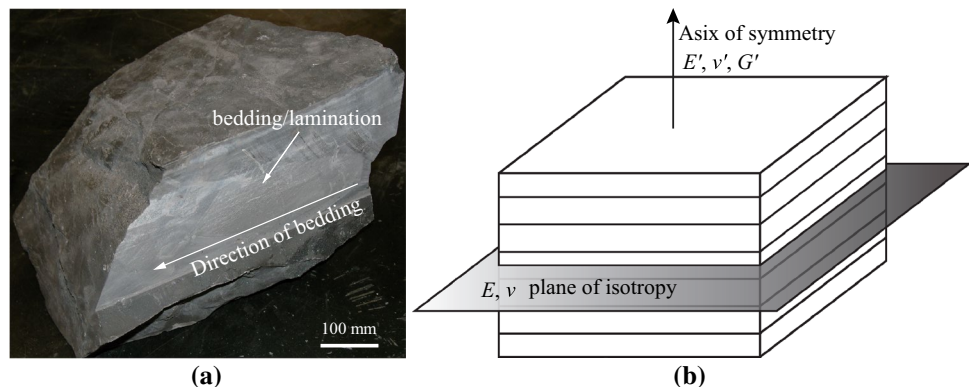
## 3 Experiments

### 3.1 Material Characterization

The shale material used in the current study was taken from outcrops of the Marcellus formation. The blocks were black and compact featuring alternating light and dark layers, as illustrated in Fig. 4a. Visual inspection showed that the shale block was free of macroscopic surface cracks and voids. The sample could be considered to be dry as the water content by mass measured by following ASTM D2216 was less than 0.2%. The average mass density was  $2558 \text{ kg/m}^3$ . The relevant mineralogy data can be found in Akono and Kabir (2018).

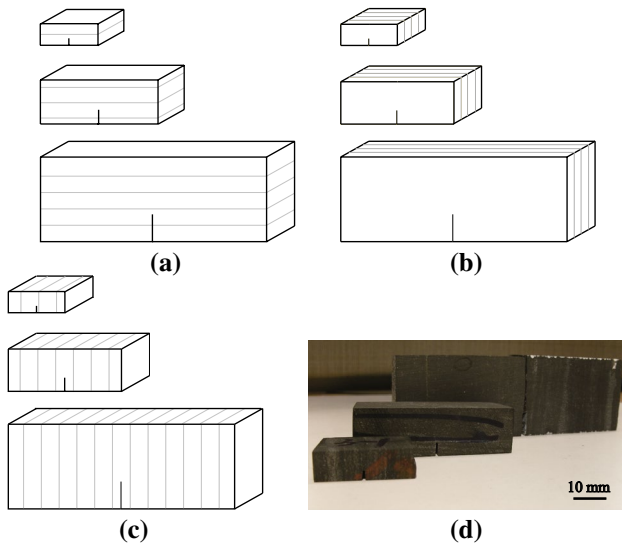
A basic characterization of the mechanical properties was carried out and included seismic velocity measurements, direct tension, uniaxial compression, and splitting tests, as reported in Jin et al. (2018). Material anisotropy was observed for seismic velocity, other elastic properties, and strength under tensile and compressive loading conditions. The test results revealed that the elastic behavior of Marcellus shale can be idealized as transversely isotropic, with the plane of isotropy coinciding with the plane of sedimentary layering, as shown in Fig. 4b. The relevant five independent elastic constants,  $E$ ,  $E'$ ,  $\nu$ ,  $\nu'$ , and  $G'$  are listed in Table 1.  $E$  and  $\nu$  are Young's modulus and Poisson's ratio, respectively, in the plane of isotropy;  $E'$  and  $\nu'$  are Young's modulus and Poisson's ratio, respectively, in the direction perpendicular to the isotropy plane;  $G'$  is the out-of-plane shear modulus.

**Fig. 4** **a** Shale block from Marcellus outcrop. **b** Transverse isotropy model and corresponding elastic constants



**Table 1** Elastic properties of Marcellus shale

Description	Symbol (units)	Measured value
In-plane modulus	$E$ (GPa)	37.7
In-plane Poisson's ratio	$\nu$ (-)	0.25
Out-of-plane modulus	$E'$ (GPa)	16.1
Out-of-plane Poisson's ratio	$\nu'$ (-)	0.35
Out-of-plane shear modulus	$G'$ (GPa)	6.9

**Fig. 5** Sketch of the specimens with three principal notch orientations: **a** arrester, **b** divider, and **c** short-transverse. **d** Picture of some of the tested specimens of different sizes

### 3.2 Specimen Preparation

The large shale block was first cut into small pieces using a table tile saw with a diamond blade. A TechCut 5<sup>TM</sup> precision sectioning machine was used to prepare three-point-bending (TPB) specimens according to the geometry reported in Fig. 1. A diamond wafering blade with thickness of 0.36 mm was used to machine the notches to a target dimensionless depth  $\alpha_0 = 0.28$ . Following the pioneering work by Schmidt (1977) and Chong et al. (1987), the specimens were made in such a way that the notches were aligned with one of the three principal orientations with respect to the isotropy plane, known as arrester, divider, and short-transverse, as depicted in Fig. 5a–c, respectively. To perform size effect tests, geometrically similar specimens of three sizes (small, medium, and large) were prepared for each specimen configuration and with size ratios of 1:2:4. Since only two-dimensional (2D) similarity was considered in this study, all the specimens had the same thickness. The larger specimens were prepared first. Pieces were collected after the larger ones broke under three-point-bend loading. To

reduce machining effort and to minimize the inevitable random scatter of material properties due to shale heterogeneity, the small- and medium-sized specimens were obtained from the collected pieces of the large specimens. Due to the stress concentration at the notch tip, the material away from the notch that was used to machine the small and medium specimens experienced very low level of stress during the tests of the large specimens and, consequently, they were considered to be free of any damage from the initial test. Typical TPB specimens with varying sizes are shown in Fig. 5d, and the detailed specimen dimensions are listed in Table 2.

Table 2 shows a certain variability of the various geometric quantities due to machining inaccuracy. In particular, the largest machining error can be observed in terms of notch length,  $a_0$ , which was the shortest dimension to machine. To check the degree of violation of the geometric similarity condition due to the notch-machining inaccuracy, an accurate measurement of the notch length was taken post-mortem. The values are listed in the fifth column of Table 2. The table also reports the notch-machining error,  $\text{MAPE}_{a_0}$ , which was estimated from the measured and designated values of  $a_0$  by means of the mean absolute percentage error (MAPE) calculation. As one can see, the  $\text{MAPE}_{a_0}$  is not always negligible (as high as 20%) leading to a violation of the geometric similarity condition. The effect of this deviation on the results will be discussed later in this paper.

### 3.3 Test Description

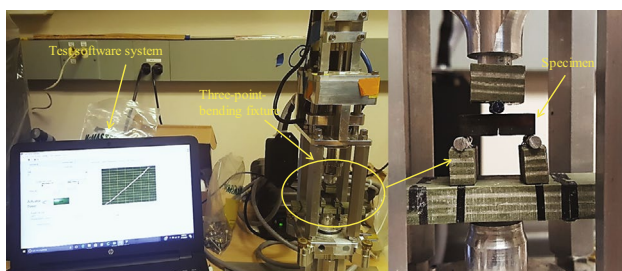
The prepared TPB specimens were placed on two supporting pins with the support span,  $S$ , equal to 74, 37, and 18.5 mm for large, medium, and small size, respectively, and were loaded vertically under symmetric three-point bending (see Fig. 6). The tests were conducted with displacement (stroke) control in a closed-loop controlled Mini-Tester with a load cell operating in the 889.64 N (200 lb) range. A constant displacement rate of 0.1, 0.05, and 0.025 mm/min was used for large, medium, and small specimens, respectively, to ensure the same strain rate for all investigated specimens. Each test lasted around 5 min to complete. The load-line displacement and the applied load were recorded during each test with a system acquisition frequency of 1 Hz. In total, 27 tests were conducted with three tests for each specimen size and configuration.

### 3.4 Experimental Results

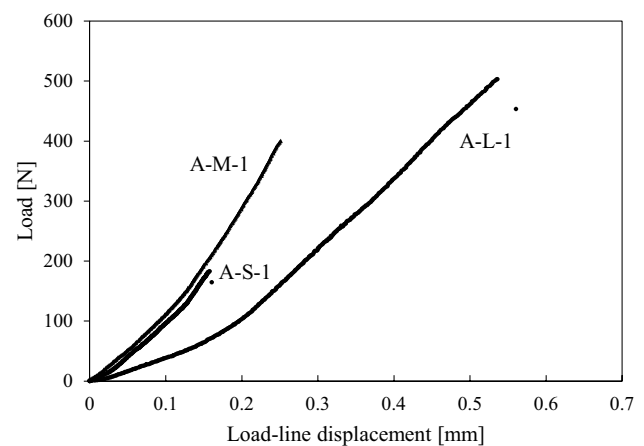
The typical load–displacement curves recorded in the experiments for three sampled specimens (one for each size) are shown in Fig. 7. The curves feature an initial stage with a gentle slope, followed by a linear segment and a subsequent sudden drop of load as soon as the peak value was reached. The gentle slope of the initial stage arises from the

**Table 2** Geometrical specifications of the TPB specimens under study

Type	Size	Specimen no.	Depth, $D$ (mm)	Thickness, $t$ (mm)	Notch length, $a_0$ (mm)	Dimensionless notch length, $\alpha_0$ (-)	Notch-machining error, $MAPE_{a_0}$ (%)
Arrester	Large	A-L-1	25.20	14.01	7.02	0.279	4.82
		A-L-2	24.23	13.45	6.39	0.264	
		A-L-3	24.47	13.75	7.41	0.303	
	Medium	A-M-1	12.52	13.81	3.47	0.277	13.4
		A-M-2	12.13	14.25	4.59	0.378	
		A-M-3	12.33	13.14	3.59	0.291	
	Small	A-S-1	6.13	13.98	2.16	0.352	20.0
		A-S-2	5.98	14.36	2.01	0.336	
		A-S-3	6.16	12.12	1.97	0.320	
Divider	Large	D-L-1	25.6	12.59	7.16	0.280	5.28
		D-L-2	25.52	12.92	7.30	0.286	
		D-L-3	23.9	13.86	7.60	0.318	
	Medium	D-M-1	12.7	12.86	3.55	0.280	7.64
		D-M-2	12.48	13.02	3.05	0.244	
		D-M-3	11.91	14.42	3.00	0.252	
	Small	D-S-1	6.41	12.70	1.65	0.257	5.47
		D-S-2	6.26	13.04	1.78	0.284	
		D-S-3	6.02	14.14	1.80	0.299	
Short-transverse	Large	ST-L-1	26.12	14.10	7.04	0.270	6.40
		ST-L-2	26.2	14.00	6.40	0.244	
		ST-L-3	25.69	14.40	7.00	0.272	
	Medium	ST-M-1	13.16	14.20	3.63	0.276	2.33
		ST-M-2	13.1	14.01	3.66	0.279	
		ST-M-3	12.72	14.55	3.75	0.295	
	Small	ST-S-1	6.54	14.07	1.91	0.292	4.29
		ST-S-2	6.57	14.04	1.73	0.263	
		ST-S-3	6.44	14.57	1.85	0.287	

**Fig. 6** Setup of the loading and data acquisition systems. The loading system consists of a load frame, a three-point-bending fixture, and a test software; the test data were collected through the test software

progressive contact between the specimen and the loading pins. The pre-peak linear segment indicates that no apparent plastic deformation takes place within the tested shale specimens. After reaching the peak load, the load–displacement curves dropped suddenly for all investigated sizes and configurations. As a consequence, the specimens failed and

**Fig. 7** Typical load–displacement curves recorded in the experiments

split into two pieces right after the peak load. This sudden failure is quite typical in this type of tests when the control variable is the machine stroke (displacement of the actuator). This is because the stroke also includes the deformability of the entire loading system, which leads to a load–displacement curve featuring snap-back. This issue was analyzed in detail by Hudson et al. (1972), Wendner et al. (2015), and Salviato et al. (2016a), among many others. A more gradual post-peak behavior could be achieved by conducting the tests under crack mouth opening displacement (CMOD) control, which, however, requires additional specimen preparation to attach a CMOD transducer to the specimens. CMOD control was not pursued in this study, because the size effect method requires measurements of peak loads only.

Furthermore, it is important to clarify that the brittle failure behavior observed in the tests does not provide information on the brittleness or quasi-brittleness of the material, but it only indicates a loss of stability of the specific tests in the post-peak regime. Indeed, as mentioned

above, stability and controllability of a fracture test depend not only on the material properties, but also on other factors such as machine frame stiffness, control loop feedback mechanism, controller settings, and specimen geometry (Salviato et al. 2016a).

The test results for the notched specimens are summarized in Table 3. The reported nominal strength,  $\sigma_{Nu}$ , was computed from the peak load with the formula reported in Sect. 2.1 (see Eq. 2). The apparent fracture toughness,  $K_{IcA}$ , and the apparent fracture energy,  $G_{IcA}$ , were calculated from the measured nominal strength according to LEFM:  $G_{IcA} = g_0 D \sigma_{Nu}^2 / E^*$  and  $K_{IcA} = (g_0 D \sigma_{Nu}^2)^{1/2}$  (see Eq. 3). The values of mean and standard deviation (SD) were calculated on the basis of the three independent tests performed for each size and each notch orientation. The results show that the apparent fracture properties depend not only on the notch orientation due to the effect of material anisotropy but also on the specimen size. This is an indication that the fracture behavior of Marcellus shale

**Table 3** Results of three-point-bending tests on Marcellus shale specimens

Type	Size	Specimen no.	Peak load $P_u$ (N)	Nominal strength, $\sigma_{Nu}$ (MPa)	Apparent fracture toughness, $\bar{K}_{IcA} \pm SD$ (MPa $\sqrt{m}$ )	Apparent fracture energy, $\bar{G}_{IcA} \pm SD$ (N/m)		
Arrester	Large	A-L-1	503.67	6.28	0.851 $\pm$ 0.055	25.344 $\pm$ 3.250		
		A-L-2	416.60	5.86				
		A-L-3	429.80	5.79				
	Medium	A-M-1	281.00	7.20			0.837 $\pm$ 0.143	24.904 $\pm$ 8.671
		A-M-2	232.78	6.16				
		A-M-3	348.17	9.67				
	Small	A-S-1	183.02	9.67			0.720 $\pm$ 0.093	18.292 $\pm$ 4.793
		A-S-2	159.70	8.63				
		A-S-3	135.98	8.20				
Divider	Large	D-L-1	498.03	6.70	0.967 $\pm$ 0.045	24.815 $\pm$ 2.291		
		D-L-2	503.39	6.64				
		D-L-3	413.71	5.80				
	Medium	D-M-1	293.00	7.84			0.852 $\pm$ 0.033	19.272 $\pm$ 1.482
		D-M-2	341.60	9.35				
		D-M-3	338.65	9.19				
	Small	D-S-1	173.31	9.22			0.675 $\pm$ 0.050	12.121 $\pm$ 1.810
		D-S-2	182.28	9.90				
		D-S-3	159.32	8.63				
Short-Transverse	Large	ST-L-1	488.98	5.64	0.820 $\pm$ 0.043	35.913 $\pm$ 3.714		
		ST-L-2	473.93	5.47				
		ST-L-3	481.68	5.63				
	Medium	ST-M-1	310.19	7.00			0.768 $\pm$ 0.010	31.486 $\pm$ 0.819
		ST-M-2	309.03	7.13				
		ST-M-3	292.47	6.90				
	Small	ST-S-1	171.78	7.92			0.642 $\pm$ 0.049	22.084 $\pm$ 3.437
		ST-S-2	177.02	8.11				
		ST-S-3	194.61	8.94				



deviates from LEFM and must be analyzed with nonlinear fracture theories.

## 4 Size Effect Analysis of the Experimental Data

### 4.1 Fitting of Size Effect Data

The identification of the fracture properties,  $c_f$  and  $G_{Ic}$ , can be obtained by fitting the experimental nominal strength by means of Bažant’s SEL (Eq. 7) through either linear or nonlinear regression approaches (Bažant and Li 1996; Tang et al. 1996). Although these two approaches are not completely equivalent, because they imply different weights of the data points, Tang et al. (1996) showed that the results obtained through the two approaches are the same when the number of test specimens increases. In this work, the linear approach is preferred and was adopted in this paper because of its simplicity. For the linear regression approach, it is convenient to write Eq. (7) in the form:

$$Y_1 = A_1 X_1 + C_1, \tag{9}$$

where  $X_1 = g_0 D/g'_0$ ,  $Y_1 = 1/g'_0 \sigma_{Nu}^2$ ,  $A_1 = 1/(E^* G_{Ic})$ ,  $C_1 = c_f/(E^* G_{Ic})$  or

$$Y_2 = A_2 X_2 + C_2, \tag{10}$$

where  $X_2 = D$ ,  $Y_2 = \sigma_{Nu}^{-2}$ ,  $A_2 = g_0/(E^* G_{Ic})$ ,  $C_2 = g'_0 c_f/(E^* G_{Ic})$ .

Equation (9) is general and can be applied even to non-similar specimens provided that the correct  $g_0$  and  $g'_0$  are calculated for each individual specimen. On the contrary, Eq. (10) can be applied only to geometrically similar specimens for which  $g_0$  and  $g'_0$  do not vary from specimen to specimen. The fitting of the experimental data with Eq. (9) (or Eq. 10) allows one to compute  $A_1$  and  $C_1$  (or  $A_2$  and  $C_2$ ), which, in turn, permits one to calculate  $c_f$  and  $G_{Ic}$ .

As mentioned earlier, the tested specimens are not exactly geometrically similar, because the actual geometry of each specimen deviates slightly from the designed geometry due to machining inaccuracies. The linear regression analysis was carried out with two approaches for comparison. The first, hereafter referred to as “method 1”, is based on Eq. (9) and takes into account the variation in the geometry of the specimens; the second, hereafter referred to as “method 2”, is based on Eq. (10), instead, and uses the designed geometry of the specimens to compute  $g_0$  and  $g'_0$ .

### 4.2 Calculation of $g(\alpha)$ and $g'(\alpha)$

The dimensionless energy release rate,  $g(\alpha)$ , can be obtained by means of Eq. (4) if the function  $\xi(\alpha, \psi, \rho)$  is known. Bao et al. (1992) proposed formulae to estimate  $\xi(\cdot)$  for a family of notched bars, which, however, do not include the case

of TPB specimens. For this reason, the function  $g(\alpha)$  was calculated numerically by finite-element analysis (FEA) in Abaqus Implicit (ABAQUS 2013).

The specimens were modeled with eight-node quadratic plane stress quadrilateral elements (CPS8) and the singularity field at the notch tip was modeled through the quarter element technique (Barsoum 1974). A linear elastic transversely isotropic constitutive model was used with the material properties reported in Table 1. The  $J$ -integral approach was adopted to estimate the energy release rate  $G$ , and the corresponding dimensionless energy release rate  $g$  was calculated according to Eq. (3). To formulate  $g$  as a function of  $\alpha$ , the simulations were performed with various dimensionless crack lengths set equal to the notch lengths,  $\alpha = \alpha_0$ , with values ranging from 0.25 to 0.32 with increments of 0.01.

Following Bažant and Planas (1997) and Guinea et al. (1998), the numerical results were interpolated with the following formula:

$$g(\alpha) = \alpha \frac{p(\alpha)^2}{(1 + 2\alpha)^2(1 - \alpha)^3}, \tag{11}$$

where  $p(\alpha)$  is a fourth-degree polynomial function. The interpolation of the numerical results resulted in  $p(\alpha) = -8.5776\alpha^4 + 7.6463\alpha^3 - 0.8044\alpha^2 - 0.6373\alpha + 1.7521$  for the arrester configuration;  $p(\alpha) = 83.079\alpha^4 - 95.591\alpha^3 + 42.436\alpha^2 - 8.5696\alpha + 2.3243$  for the divider configuration;  $p(\alpha) = 168.61\alpha^4 - 197.05\alpha^3 + 87.288\alpha^2 - 17.357\alpha + 3.0228$  for the short-transverse configuration. Figure 8a–c shows the comparison between the numerical results and the functions  $p(\alpha)$ . Clearly, the fourth-order polynomial function provides a very accurate fit of the numerical results for all notch configurations.

Finally,  $g'(\alpha)$  can be computed by direct derivation of  $g(\alpha)$ . One gets

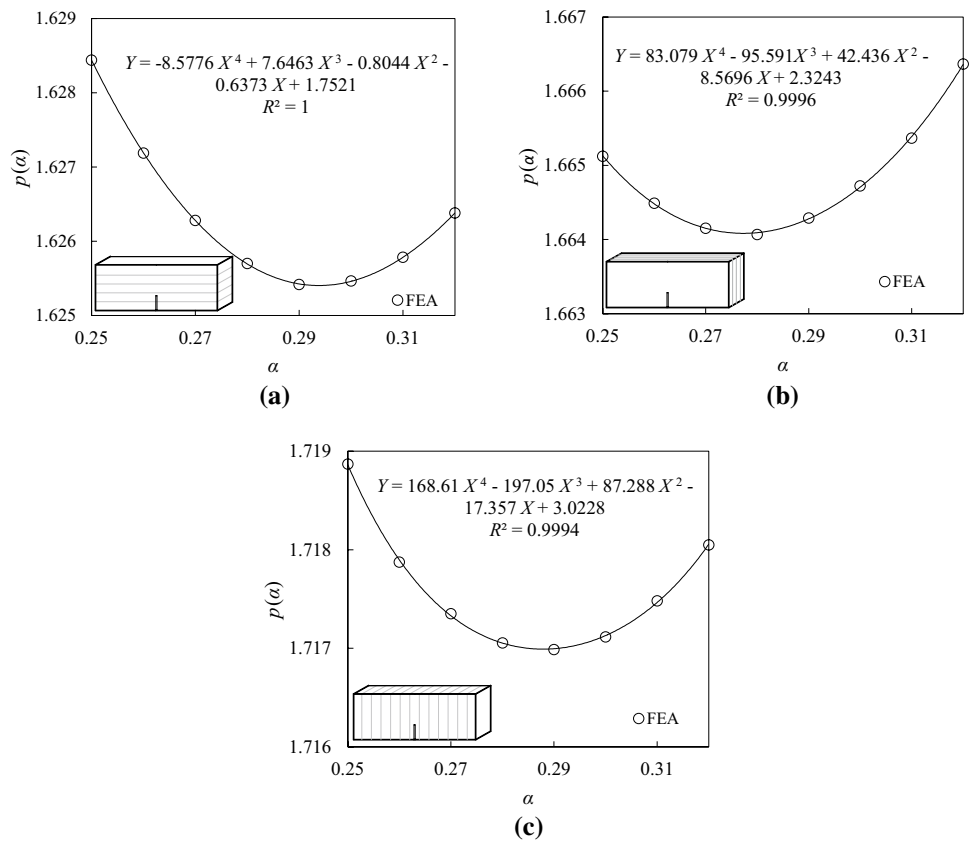
$$g'(\alpha) = (8\alpha^2 + 1) \frac{p^2(\alpha)}{(\alpha - 1)^4(2\alpha + 1)^3} + \alpha \frac{2p(\alpha)p'(\alpha)}{(1 - \alpha)^3(2\alpha + 1)^2}. \tag{12}$$

With regard to the values of  $g$  and  $g'$  for a specific specimen required for the linear regression analysis,  $\alpha$  takes the value of  $\alpha_0$  at the beginning of crack propagation, i.e.,  $g_0 = g(\alpha_0)$  and  $g'_0 = g'(\alpha_0)$ .

### 4.3 Identification of Fracture Properties

The linear regression analysis for both method 1 and method 2 was conducted by means of the classical least square method. The results of the regression analysis as well as the experimental data are presented in Fig. 9a–c for the arrester, divider, and short-transverse configurations, respectively, for method 1; and in Fig. 10a–c, for method 2. The regression analysis provides a mean estimate of slope,  $\bar{A}_i$ , and intercept,  $\bar{C}_i$ , of the straight line as well as

**Fig. 8** Calculation of the function  $p(\alpha)$ , defining the dimensionless energy release rate according to Eq. (11), by a fourth-degree polynomial interpolation of the FEA solutions for the investigated **a** arrester, **b** divider, and **c** short-transverse configurations



their standard error (SE),  $SE_{A_i}$  and  $SE_{C_i}$ , where  $i = 1$  for method 1 and  $i = 2$  for method 2.

The mean and SE values of the regression parameters can then be used to compute mean and SE for the fracture properties. Considering the relation between the fracture properties and the regression parameters, and according to the second-order formulae for the statistics of a function of several random variables (Elishakoff 1983), one can write

$$\bar{G}_{Ic}^i = \frac{1}{E^* \bar{A}_i} \left( 1 + \frac{n(SE_A^i)^2}{\bar{A}_i^2} \right), \quad \bar{c}_f^i = E^* \bar{C}_i \bar{G}_{Ic}^i \quad (13a)$$

$$SE_{G_{Ic}}^i = \frac{SE_A^i}{E^* \bar{A}_i^2}, \quad SE_{c_f}^i = \sqrt{\frac{(SE_C^i)^2}{\bar{A}_i^2} + \frac{\bar{C}_i^2 (SE_A^i)^2}{\bar{A}_i^4}}, \quad (13b)$$

in which  $A_i$  and  $C_i$  are assumed to be statistically independent,  $1 + n(SE_A^i)^2/\bar{A}_i^2 \approx 1$ ,  $n$  represents the number of the data points, and, again,  $i = 1$  for method 1 and  $i = 2$  for method 2. The results are reported in Table 4 along with the values of the coefficient of determination (denoted by  $R^2$ ) and the root-mean-squared error (RMSE) of the estimate based on the errors of prediction, both of which characterize the accuracy of the fit.

By comparing the fitting results of method 1 and 2, one can clearly see that a better fitting of the experimental data was obtained by means of method 1. In particular, one can see that the RMSE values are almost one order of magnitude smaller for method 1 than for method 2. Given that the random errors in measurement and regression due to material heterogeneity and other random factors are the same in these two methods, the greater fitting errors for method 2 must be attributed to the fact that it fails to incorporate the effect of the machining errors, which occurred in the notch preparation processes. The machining errors propagate eventually to the calculations of  $g$  and  $g'$  at a fixed designated  $\alpha_0$ . This can be also shown by comparing the fitting results of the specimens with different configurations. Indeed, the results show that larger notch-machining errors (see  $MAPE_{a_0}$  values in Table 2) correspond to greater fitting errors (see  $R^2$  and RMSE values in Table 4). Method 1 does not suffer from the machining errors, because the geometrical similarity of the specimens is not required. Table 4 shows also that  $SE_{c_f}$  is about two orders of magnitude larger than  $SE_{G_{Ic}}$  in all the cases. This demonstrates that  $c_f$  is more susceptible to errors compared to  $G_{Ic}$  under the error normality assumption.

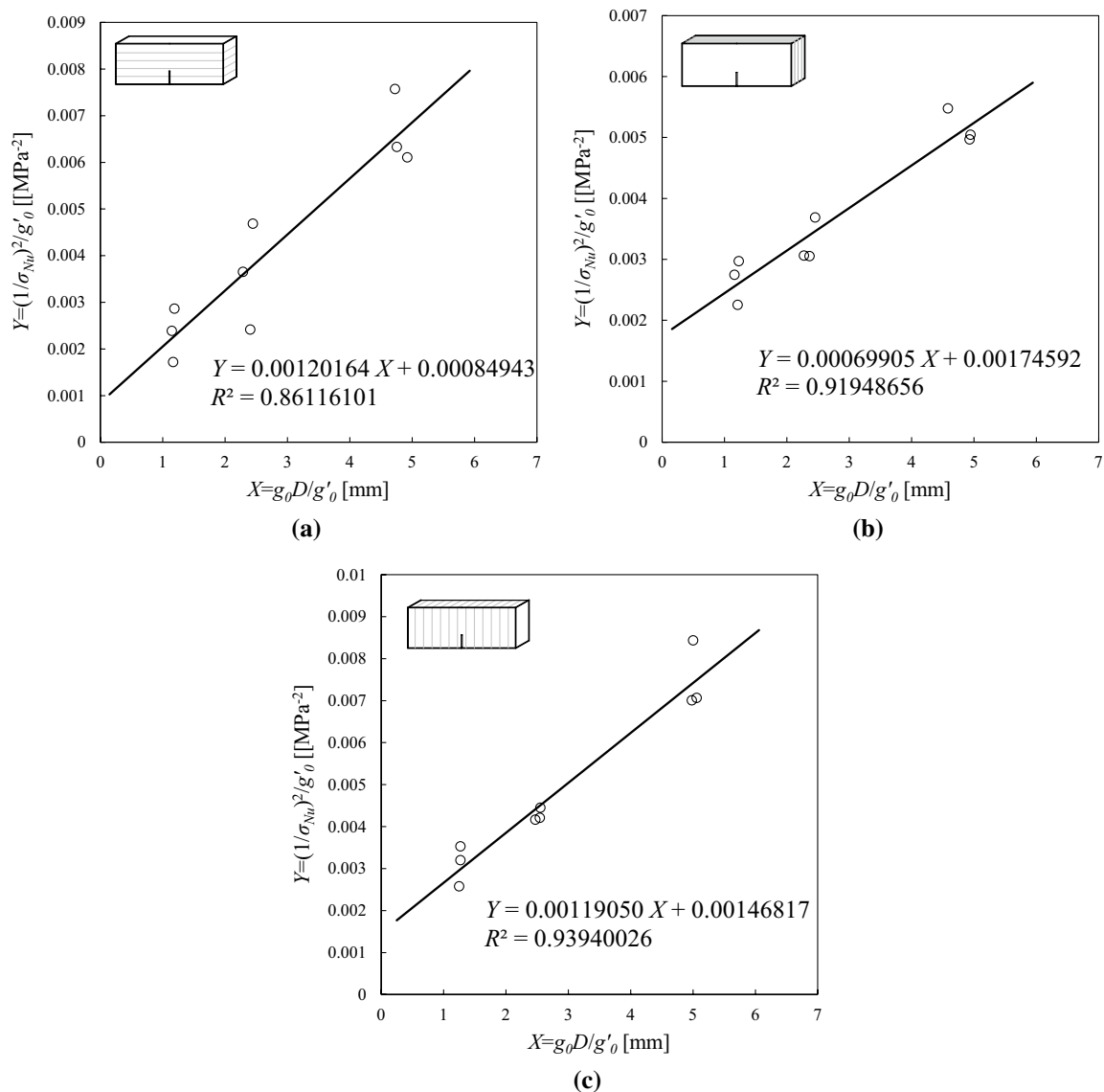


**Fig. 9** Linear regression analysis of the experimental nominal strength data relevant to various specimen sizes based on method 1 (see Eq. 9) for **a** arrester, **b** divider, and **c** short-transverse configurations

Further discussions are based on the fitting results of method 1, since it provided more accurate estimates of the fracture properties of the material.

#### 4.4 Size Effect on the Nominal Strength

The experimental data on the nominal strength are reported in Fig. 11 where the normalized nominal strength,  $\sigma_{Nu}/\sigma_0$ , is plotted as a function of the brittleness number,  $\beta = D/D_0$ , with a double logarithmic scale. Since the brittleness number accounts for both size effect, through  $D$ , and geometry effect, through  $D_0$  (see Sect. 2.1), Fig. 11 allows one to compare the different configurations (notch orientations with respect to the shale plane of isotropy).

As one can see, the experimental data agree well with Bažant’s SEL regardless of the configuration. The SEL provides a smooth transition from the strength criterion characterized by a horizontal asymptote for  $\beta \rightarrow 0$ , in which no size effect on nominal strength is expected (ductile behavior), to LEFM characterized by an inclined asymptote of slope  $- 1/2$  for  $\beta \rightarrow \infty$  (brittle behavior). Note that the larger the brittleness number  $\beta$ , the closer the corresponding structure is to the LEFM asymptote. Hence, the term *brittleness* must be understood here as the proximity to the LEFM scaling.

Instead, quasi-brittle behavior occurs for  $\beta$  values in the transition zone typically identified as  $0.1 \leq \beta \leq 10$ . The  $\beta$  values for all the investigated specimens in this work fall

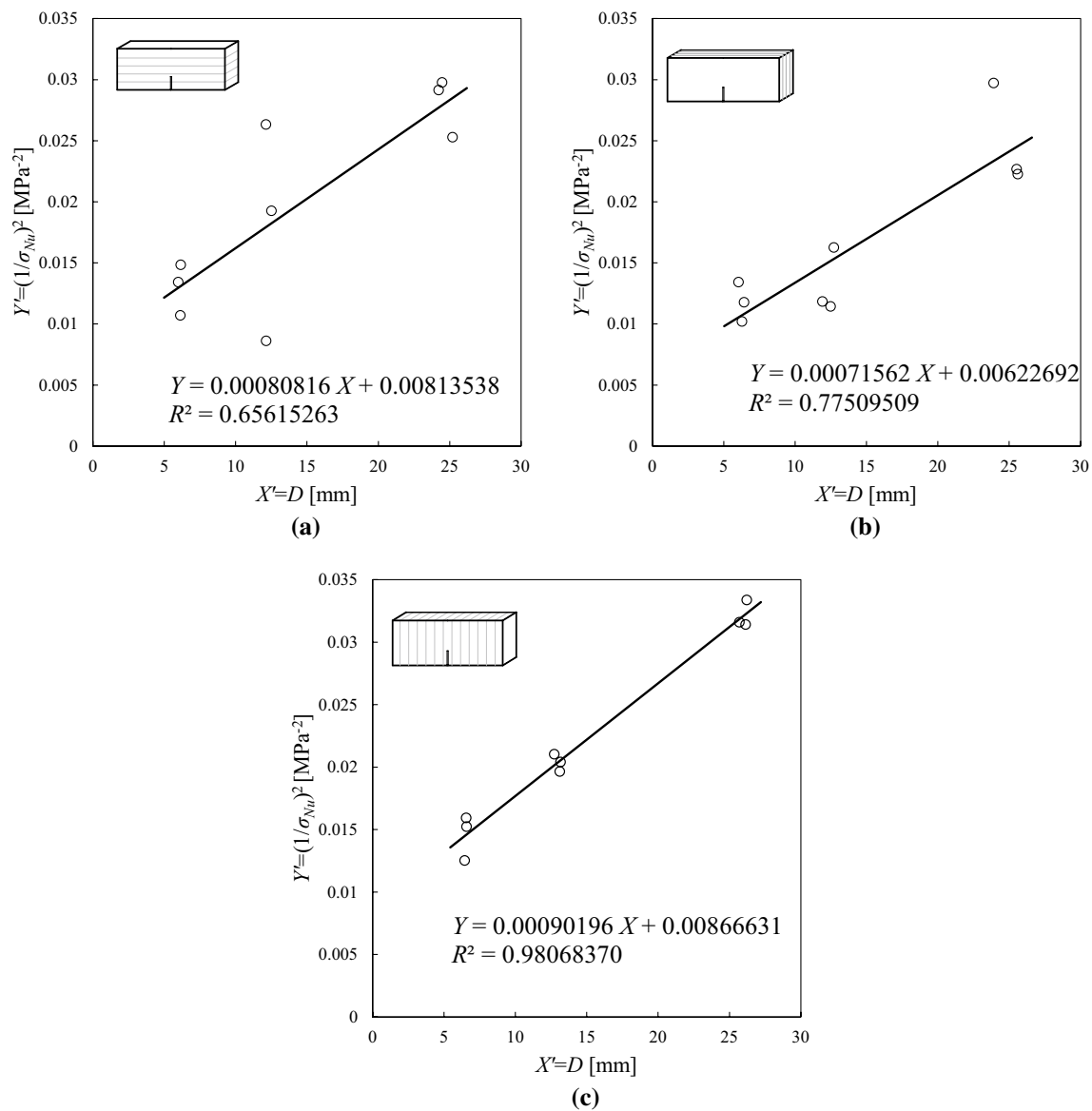


**Fig. 10** Linear regression analysis of the experimental nominal strength data relevant to various specimen sizes based on method 2 (see Eq. 10) for **a** arrester, **b** divider, and **c** short-transverse configurations

**Table 4** Calculated fracture properties based on the size effect method

Method	Type	$R^2$	RMSE	$G_{Ic}$ (N/m)	$SE_{Gf}$	$c_f$ (mm)	$SE_{cf}$
1	Arrester	0.861	0.000827	29.0	0.00440	0.731	0.492
1	Divider	0.919	0.000355	37.9	0.00424	2.99	0.452
1	Short-Tran.	0.939	0.000534	44.8	0.00430	1.23	0.340
2	Arrester	0.656	0.00512	35.1	0.00962	0.194	1.02
2	Divider	0.775	0.00342	31.6	0.00644	1.68	0.734
2	Short-Tran.	0.981	0.00116	53.7	0.00285	1.86	0.203

within the range of 0.4–6.8, which are in the transition zone, as shown in Fig. 11. Therefore, the fracture behavior of shale

must be regarded as quasi-brittle, and neither a strength criterion nor LEFM can be used for its description.

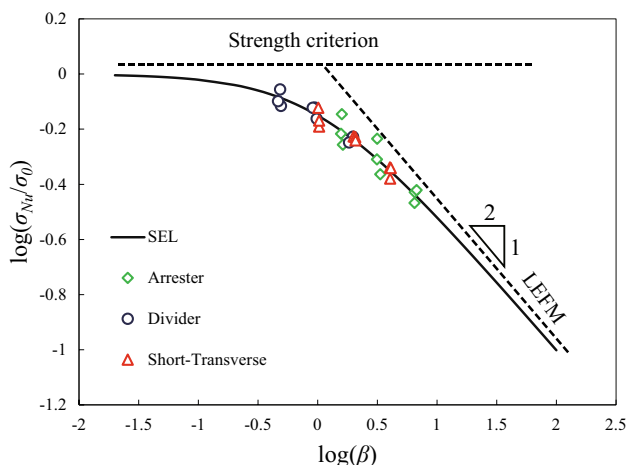


**Fig. 11** Comparison of experimental data for all the configurations with Bažant’s SEL. The nominal strengths  $\sigma_{Nt}$  are normalized by  $\sigma_0$  and plotted against the brittleness number  $\beta = D/D_0$  on a double logarithmic scale

### 4.5 Size Effect on the Apparent Fracture Toughness

The term fracture toughness is widely used in the literature for both laboratory and field studies with implicit reference to LEFM. However, as we have discussed in this paper, there is plenty of confusion between fracture toughness as a unique material characteristic, which does not depend on the testing method and the specimen size, and the apparent fracture toughness as a “structural” property, which, however, is measured with reference to a specific specimen size and a specific geometry. The confusion can be clarified through the study of its size and geometry dependency similar to the discussion in Bažant et al. (1991). As previously done in this paper, it is convenient to denote the apparent fracture toughness calculated using LEFM by  $K_{IcA}$  and to denote the fracture toughness of the material by  $K_{Ic}$ .

The normalized apparent fracture toughness of the investigated specimens,  $K_{IcA}/K_{Ic}$ , can be plotted against the corresponding brittleness number,  $\beta$ , as shown in Fig. 12. The value of  $K_{IcA}$  was calculated according to Eq. (1) by setting  $\sigma_N = \sigma_{Nt}$ , and  $K_{Ic}$  was calculated as  $K_{Ic} = \sqrt{E^*G_{Ic}}$ . With the values of  $G_{Ic}$  reported in Table 4, one has  $K_{Ic} = 0.912, 1.20,$  and  $0.917 \text{ MPa}\sqrt{\text{m}}$  for the arrester, divider, and short-transverse configurations, respectively. It can be seen from Fig. 12 that, for the specimens with a larger brittleness number, a greater apparent fracture toughness was obtained. Specifically, for geometrically scaled specimens of the same type,  $K_{IcA}$  increases with the brittleness number or, equivalently, the specimen size  $D$ . This observation is in agreement with the fracture tests on different types of rocks available in the literature (Bocca et al. 1989; Bažant and Kazemi 1990a; Bažant et al. 1991; Ayatollahi and Akbar-doust 2014; Kataoka and Obara 2015).

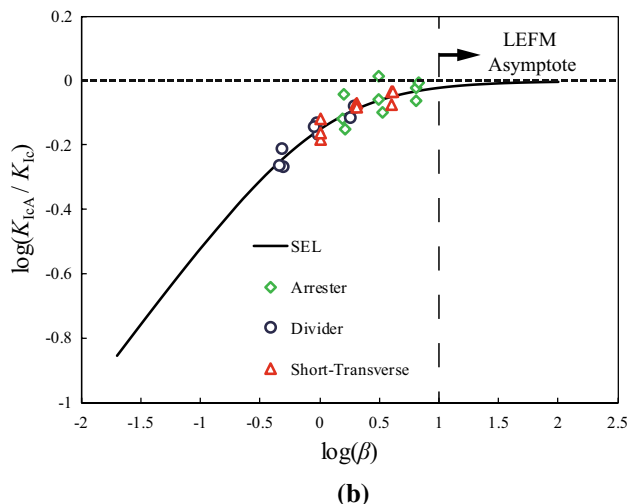
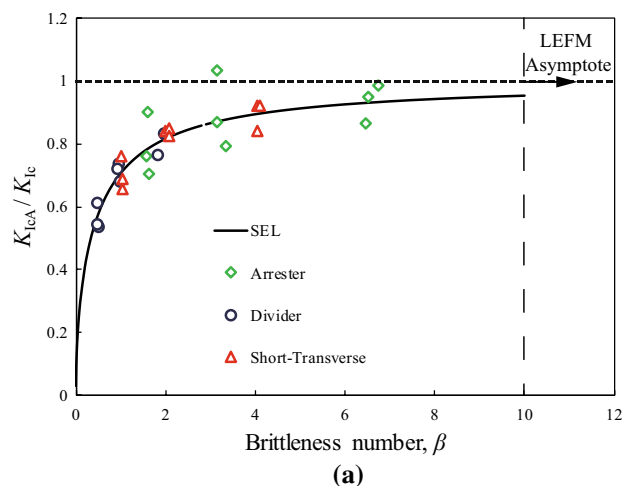


**Fig. 12** Variation of normalized apparent fracture toughness  $K_{IcA}/K_{Ic}$  as a function of the brittleness number  $\beta$  on **a** a linear scale and **b** a double logarithmic scale. The fracture toughness of the material  $K_{Ic}$  can be approximated by  $K_{IcA}$  (i.e.,  $K_{IcA} \approx K_{Ic}$ ) only when  $\beta$  is sufficiently large ( $\beta > 10$ )

The variation of  $K_{IcA}$  as a function of  $\beta$  can be predicted also by the SEL. Substituting Eqs. (8) and (4) into Eq. (1) with  $\sigma_N = \sigma_{Nt}$  and  $K_{Ic} = \sqrt{E^*G_{Ic}}$ , one obtain

$$\frac{K_{IcA}}{K_{Ic}} = \sqrt{\frac{\beta}{1 + \beta}} \tag{14}$$

Equation 14 is also plotted as a solid line in Fig. 12. The agreement between the predicted trend and the experimental data is excellent. The ratio of  $K_{IcA}$  to  $K_{Ic}$  gradually increases as  $\beta$  increases and eventually converges to the asymptotic value 1 as  $\beta \rightarrow \infty$ . In other words, unless the tested specimen is sufficiently large, the fracture toughness of the material cannot be approximated by the apparent one. In practice,  $\beta \geq 10$  is required to apply classic LEFM and thus to

approximate  $K_{Ic}$  by  $K_{IcA}$ . For the shale material tested in this paper, specimens with  $D \geq 50$  mm for the arrester,  $D \geq 125$  mm for the divider, and  $D \geq 75$  mm for the short-transverse are required for a reasonable approximation. It is worth observing that these values depend on the intrinsic characteristic size  $D_0$  (see Sect. 2.1), which, in turn, depends on the internal structure and heterogeneity of the material. Hence, in general, the correct minimum specimen size cannot be known a priori and its identification requires size effect tests.

#### 4.6 Anisotropy of Fracture Properties

The presented results show that the Marcellus shale fracture properties are significantly anisotropic. Anisotropy of fracture properties has to be considered to determine crack deflection under complex loading, e.g., in hydraulic fracturing (Zeng and Wei 2017; Gao et al. 2017; Li et al. 2018a; Zia et al. 2018; Zeng et al. 2018). The previous studies (Schmidt 1977; Chandler et al. 2016) showed that the highest value of fracture toughness was obtained from divider specimens and the lowest one from short-transverse, i.e., divider > arrester > short-transverse. A similar conclusion can be drawn from the  $K_{IcA}$  measurements reported in this work, as listed in Table 3, for the large- and medium-sized specimens. However, this conclusion may be misleading, since the comparison was conducted based on the apparent properties measured with specific specimen size and geometry rather than the “true” properties of materials. In this sense, it is more meaningful to compare the fracture toughness calculated from the size effect tests with the corrections to the size and geometry effects. For the reported  $K_{Ic}$  values, one can see that the divider specimens exhibited the highest resistance to mode I fracture, while the values for the arrester and short-transverse configurations are similar, i.e., divider  $\gg$  short-transverse  $\approx$  arrester. In terms of fracture energy, the anisotropy of the elastic properties needs to be taken into account also considering the relation between  $G_{Ic}$  and  $K_{Ic}$  as shown in Eq. (3). From the calculated  $G_{Ic}$  reported in Table 4, one can find that short-transverse > divider > arrester.

Another important characteristic relevant to the fracture behavior of quasi-brittle materials is the FPZ length, which can be quantified by  $c_f$  (Bažant and Planas 1997), and it is strongly related to brittleness of the material. Considering that  $\beta$ , which is a measure of “structural” brittleness, is proportional to  $1/c_f$ , a material with a smaller  $c_f$  tends to be more brittle, and vice versa. Indeed, for  $c_f \rightarrow 0$ ,  $D_0 \rightarrow \infty$  and the behavior is governed by LEFM.

As shown in Table 4, the arrester specimens exhibit the shortest FPZ length, while the divider the longest. As a consequence, relatively more brittle behavior is expected for the arrester configuration given the same size and geometry. This conclusion agrees with the observation by Chandler

et al. (2016) that the arrester specimens of Mancos shale exhibited less inelasticity compared to the other ones, and the fracture tests on Anvil Point oil shale conducted by Schmidt (1977) which showed that a loss of stability occurred only for the tests on the arrester configuration.

## 5 Comparison with the Cohesive Crack Model

As discussed in Sect. 2.2, there exists a certain optimal size range in which the size effect method gives results that are fully consistent with the cohesive crack model. This aspect, often overlooked in the literature, is important for practical applications, since numerical simulations of fracture propagation in rocks are often performed with the cohesive crack model with fracturing parameters identified in laboratory tests.

All the experimental data obtained in this paper are plotted in Fig. 13 with reference to the normalized size  $X = \hat{D}$  and the normalized strength variable  $Y = (f'_t \sigma_{Nu})^2 / g'_0$ . The plot also shows the corresponding normalized SEL ( $Y = X + 0.44$ ) when  $G_{Ic} = G_f$ . As one can see, the data points correspond well to the straight line and are, for the most part, in the interval  $0.2 < \hat{D} < 2$ . Only one set of points, the one relevant to the largest size specimens tested under the arrester configuration, have  $\hat{D} > 2$ . However, even in this case, the data points do not deviate from the SEL calculated with  $G_f$ . This is an indication that the cohesive crack law for shale is most likely linear all the ways to the complete separation.

For further verification that the fracture properties calculated from the size effect tests are appropriate to be used as parameters of the cohesive crack model, numerical simulations were performed on selected specimens of

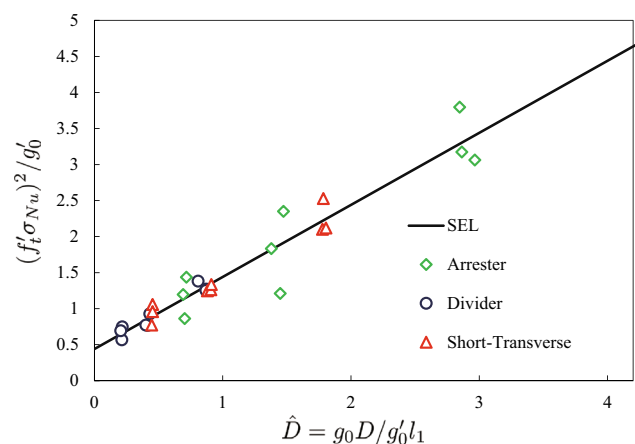


**Fig. 13** Comparison of all size effect data with Bažant’s SEL in a parametric space in which Bažant’s SEL is a straight line  $Y = X + 0.44$

increasing sizes with the standard finite-element (FE) technique (ABAQUS 2013). The material outside the notch of a simulated specimen was modeled by standard isoparametric quadratic elements and with transversely isotropic elastic constitutive equations characterized by the elastic parameters reported in Table 1. The crack line was modeled by cohesive connections with negligibly small interface thickness and governed by a linear cohesive law. The values of the fracture parameters were taken from the size effect results obtained with method 1 (see Table 4). The tensile strength was estimated on the basis of the formula  $f_t' = (E^*G_f/l_1)^{1/2}$  (see Sect. 2.2) which gives 22 MPa, 16 MPa, and 17 MPa, for the arrester, divider, and short-transverse configuration, respectively. It is worth mentioning that these values tend to be higher than the tensile strength measured with Brazilian split-cylinder tests (Li et al. 2016; Jin et al. 2018). This discrepancy has already been investigated by Cusatis and Schaffert (2009) who attributed it to an initial short plateau in the real cohesive law which is neglected by the linear cohesive law. They also verified that the tensile strength estimated from the size effect law is the correct one to use in cohesive crack simulations for large enough specimens ( $\hat{D} > 0.2$ ).

Figure 14 shows a typical FE mesh used in the calculations. The notch tip was simulated as semi-circular to avoid stress singularities that are inconsistent with the cohesive crack model, and the notch width was taken as 0.4 mm and kept constant for all sizes. This geometrical representation of the notch is the same as the one adopted by Cusatis and Schaffert (2009) who extensively studied the effect of the

stress concentration at the notch tip on the cohesive crack simulation of size effect.

The element size  $h_e$  ahead of the notch tip was selected within the relatively small range of 0.05–0.2 mm (about 1/10–1/5 of the FPZ length estimated as  $2c_f$ ) and was not scaled upward with the specimen size to ensure accurate calculation of the stress concentration and accurate resolution of the FPZ for all specimen sizes.

Table 5 reports the numerically calculated peak loads relevant to the investigated specimens along with the corresponding experimental value and the prediction error. One can see that, for all investigated specimens, the numerical predictions agree well with the experiments. This confirms once more that the size effect method does provide fracture parameters that are consistent with the cohesive crack model. In addition, the calculated cohesive stress at the notch tip corresponding to the peak load of the large specimens of various notch configurations was found to be close to zero. This validates the assumption of the fully developed FPZ as discussed in Sect. 2 and suggests that the adoption of the linear cohesive law is appropriate for the investigated shale specimens.

The simulated load–displacement curves are shown in Fig. 15. All the curves feature a steep initial post-peak, which in several of the simulations is basically vertical. With these specimen responses and if one accounts for the inevitable deformability of the test apparatus, the actually recorded load displacement curves would feature a snap-back behavior which is unstable even in displacement control (Wendner et al. 2015). This is consistent with the experimental results

**Fig. 14** Typical finite-element mesh for three-point-bending simulations. The notch width is 0.4 mm for all the simulated specimens, and the element size ahead of the notch tip ranges from 0.05 to 0.2 mm

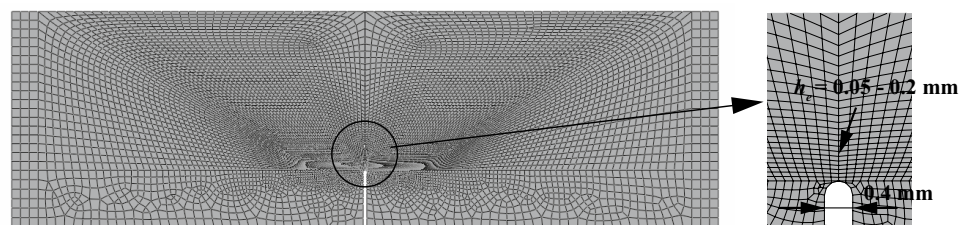


**Table 5** Comparison between experimental and numerical peak loads of the selected specimens

Type	Size	Specimen no.	Peak Load		
			Experimental (N)	Numerical (N)	Error (%)
Arrester	Large	A-L-2	416.60	451.05	8.27
	Medium	A-M-2	232.78	236.03	1.40
	Small	A-S-2	159.70	178.39	11.70
Divider	Large	D-L-1	498.03	482.04	3.21
	Medium	D-M-1	293.00	311.69	6.38
	Small	D-S-1	173.31	190.40	9.86
Short-transverse	Large	ST-L-3	481.68	510.93	6.07
	Medium	ST-M-3	292.47	312.99	7.01
	Small	ST-S-3	194.61	205.99	5.85

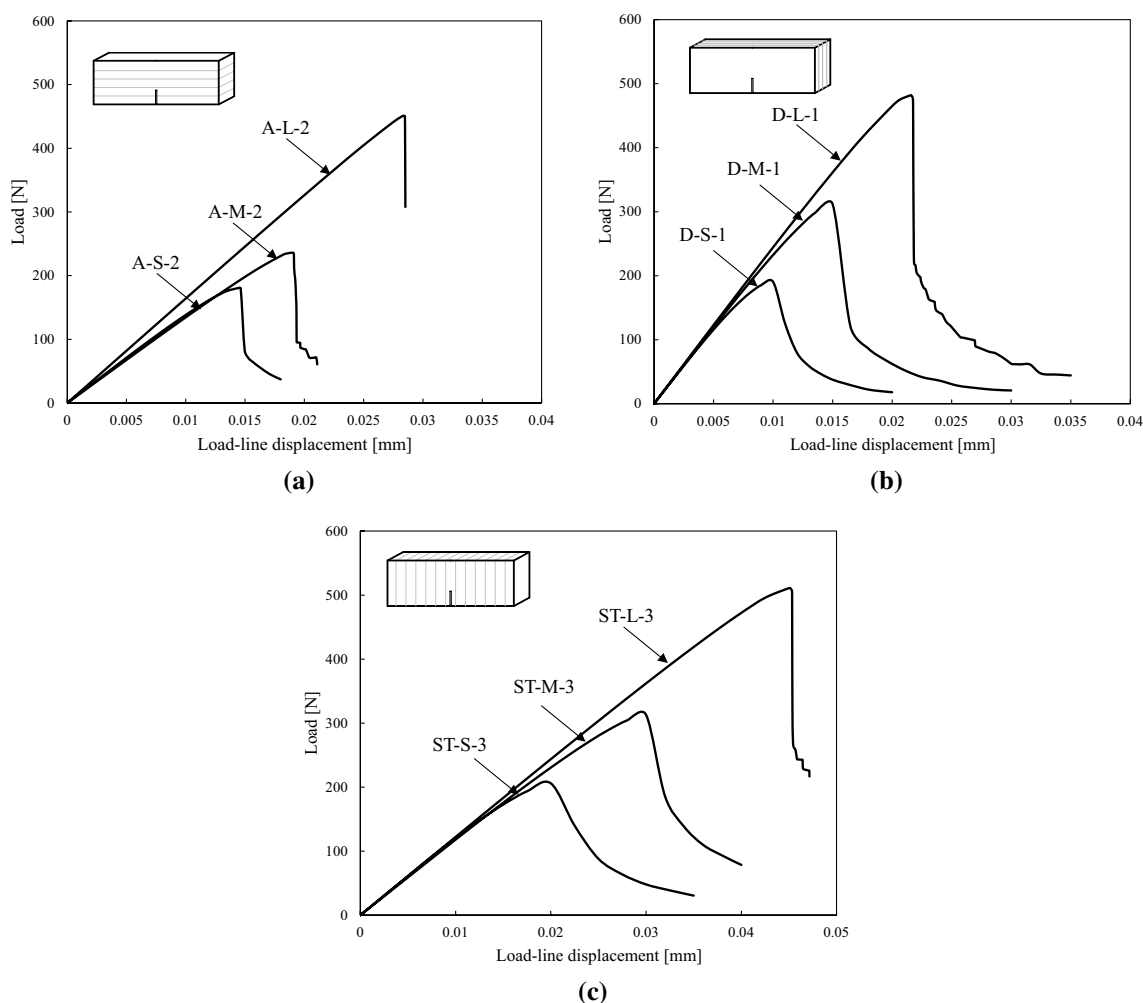


**Fig. 15** Numerical load versus displacement curves for the different sizes of the selected **a** arrester, **b** divider, and **c** short-transverse configurations

(see Fig. 7), in which (1) the initial slope of the load–displacement curve is smaller than the simulated one, because it includes the deformability of the entire system; (2) it was not possible to record the post-peak, because all the specimens failed suddenly at the peak load.

## 6 Conclusions

In this study, size effect tests were conducted on various three-point-bending (TPB) specimens of increasing size and different notch configuration to obtain the fracture properties of Marcellus shale in three principal orientations. The following conclusions can be drawn:

1. The size effect method provides an indirect way of measuring the fracture energy, the fracture toughness, and the length of the effective fracture process zone by means

of measurements of the peak loads of specimens with varying sizes and the elastic properties of the material. According to this approach, the fracture energy,  $G_{Ic}$ , of the investigated Marcellus shale was identified to range from 29.0 to 44.8 N/m depending on the notch orientation; the fracture toughness,  $K_{Ic}$ , was identified to range from 0.912 to 1.20  $\text{MPa}\sqrt{\text{m}}$ ; and the effective fracture process zone length,  $c_f$ , was identified to range from 0.731 to 2.99 mm.

2. Significant anisotropy in the obtained fracture toughness, fracture energy, and effective FPZ length was observed.
3. The size effect law (SEL) proposed by Bažant accounts for the effects of both specimen size and geometry. The geometry dependence allows one to account for the effect of machining errors in the specimen preparation. This leads to a fitting of experimental data that exhibit less scatter and reduced errors.



4. The brittleness number,  $\beta$ , can be used to quantify the brittleness of the investigated specimens, which not only depends on the material characteristics but also on the specimen size and geometry.
5. The experimental investigation shows remarkable size effect on the measured nominal strength and apparent fracture toughness. This aspect is often overlooked in the literature on shale fracture mechanics. Neither the strength-based criterion nor classic linear elastic fracture mechanics (LEFM) can predict the size effect data shown in this paper. On the contrary, the nonlinear fracture mechanics of the quasi-brittle type is applicable for fracture characterization of shale in laboratory tests and permits one to extrapolate the measured values to the values that may be used in field applications.
6. The previously demonstrated relationship between the fracture parameters of Bažant's SEL and the fracture parameters of the widely used cohesive crack model showed that the fracture energy identified with the size effect method,  $G_{lc}$ , corresponds to the initial fracture energy,  $G_f$ , of the cohesive crack model. The consistency between  $G_{lc}$  and  $G_f$  was verified numerically by means of numerical simulations. The numerically calculated peak loads using  $G_f = G_{lc}$  matched the experimental measurements very well.
7. The size effect results suggest also that, for the investigated Marcellus shale, the total fracture energy,  $G_F$ , is close to the initial value,  $G_f$ . This means that the cohesive law for shale is basically linear and does not feature any significant nonlinear "tail".

**Acknowledgements** The authors would like to thank Professor Brad Sageman (Department of Earth and Planetary Sciences, Northwestern University) for providing the Marcellus shale samples used in this study and Professor Giuseppe Buscarnera (Department of Civil and Environmental Engineering, Northwestern University) for his assistance with the Mini-Tester. This work also made use of the Materials Characterization and Imaging Facility and the Center for Sustainable Engineering of Geological and Infrastructure Materials (SEGIM) at Northwestern University.

## References

- ABAQUS (2013) ABAQUS Users Manual, Ver. 6.13-1. Dassault Systems, Providence, RI, USA
- Aicher S (2010) Process zone length and fracture energy of spruce wood in mode-I from size effect. *Wood Fiber Sci* 42(2):237–247
- Akono AT (2016) Energetic size effect law at the microscopic scale: application to progressive-load scratch testing. *J Nanomech Micromech* 6(2):04016.001
- Akono AT, Kabir P (2016) Microscopic fracture characterization of gas shale via scratch testing. *Mech Res Commun* 78:86–92
- Akono AT, Kabir P (2018) Influence of geochemistry on toughening behavior of organic-rich shale. arXiv preprint [arXiv:1804.10926](https://arxiv.org/abs/1804.10926)
- Ayatollahi M, Akbardoost J (2014) Size and geometry effects on rock fracture toughness: mode I fracture. *Rock Mech Rock Eng* 47(2):677–687
- Bao G, Ho S, Suo Z, Fan B (1992) The role of material orthotropy in fracture specimens for composites. *Int J Solids Struct* 29(9):1105–1116
- Barenblatt GI (1962) The mathematical theory of equilibrium cracks in brittle fracture. In: *Advances in applied mechanics*, vol 7, Elsevier, pp 55–129
- Barpi F, Valente S, Cravero M, Iabichino G, Fidelibus C (2012) Fracture mechanics characterization of an anisotropic geomaterial. *Eng Fract Mech* 84:111–122
- Barsoum RS (1974) Application of quadratic isoparametric finite elements in linear fracture mechanics. *Int J Fract* 10(4):603–605
- Bažant ZP (1984) Size effect in blunt fracture: concrete, rock, metal. *J Eng Mech* 110(4):518–535
- Bažant ZP, Kazemi MT (1990a) Determination of fracture energy, process zone length and brittleness number from size effect, with application to rock and concrete. *Int J Fract* 44(2):111–131
- Bažant ZP, Kazemi MT (1990b) Size effect in fracture of ceramics and its use to determine fracture energy and effective process zone length. *J Am Ceram Soc* 73(7):1841–1853
- Bažant ZP, Li Z (1996) Zero-brittleness size-effect method for one-size fracture test of concrete. *J Eng Mech* 122(5):458–468
- Bažant ZP, Pfeiffer PA (1987) Determination of fracture energy from size effect and brittleness number. *ACI Mater J* 84(6):463–480
- Bažant ZP, Planas J (1997) Fracture and size effect in concrete and other quasibrittle materials, vol 16. CRC Press, Boca Raton
- Bažant ZP, Gettu R, Kazemi MT (1991) Identification of nonlinear fracture properties from size effect tests and structural analysis based on geometry-dependent R-curves. *Int J Rock Mech Min Sci Geomech Abstr* 28(1):43–51
- Bažant ZP, Daniel IM, Li Z (1996) Size effect and fracture characteristics of composite laminates. *J Eng Mater Technol* 118:317
- Bocca P, Carpinteri A, Valente S (1989) Fracture mechanics of brick masonry: size effects and snap-back analysis. *Mater Struct* 22(5):364–373
- Cedolin L, Cusatis G (2008) Identification of concrete fracture parameters through size effect experiments. *Cement Concr Compos* 30(9):788–797
- Chandler MR, Meredith PG, Brantut N, Crawford BR (2016) Fracture toughness anisotropy in shale. *J Geophys Res Solid Earth* 121(3):1706–1729
- Chau VT, Bažant ZP, Su Y (2016) Growth model for large branched three-dimensional hydraulic crack system in gas or oil shale. *Philos Trans R Soc A* 374(2078):20150.418
- Chen X, Eichhubl P, Olson JE (2017) Effect of water on critical and subcritical fracture properties of woodford shale. *J Geophys Res Solid Earth* 122(4):2736–2750
- Chong KP, Smith JW (1984) *Mechanics of oil shale*. Elsevier, Oxford
- Chong KP, Kuruppu MD, Kuzmaul JS (1987) Fracture toughness determination of layered materials. *Eng Fract Mech* 28(1):43–54
- Chong KP, Li VC, Einstein HH (1989) Size effects, process zone and tension softening behavior in fracture of geomaterials. *Eng Fract Mech* 34(3):669–678
- Cusatis G, Schaufert EA (2009) Cohesive crack analysis of size effect. *Eng Fract Mech* 76(14):2163–2173
- Dugdale DS (1960) Yielding of steel sheets containing slits. *J Mech Phys Solids* 8(2):100–104
- Elishakoff I (1983) *Probabilistic methods in the theory of structures*. Wiley, Oxford
- Gao Y, Liu Z, Zeng Q, Wang T, Zhuang Z, Hwang KC (2017) Theoretical and numerical prediction of crack path in the material with anisotropic fracture toughness. *Eng Fract Mech* 180:330–347

- Guinea G, Pastor J, Planas J, Elices M (1998) Stress intensity factor, compliance and  $cmod$  for a general three-point-bend beam. *Int J Fract* 89(2):103–116
- Hillerborg A, Mod er M, Petersson PE (1976) Analysis of crack formation and crack growth in concrete by means of fracture mechanics and finite elements. *Cem Concr Res* 6(6):773–781
- Hubler MH, Ulm FJ (2016) Size-effect law for scratch tests of axisymmetric shape. *J Eng Mech* 142(12):04016,094
- Hudson JA, Crouch SL, Fairhurst C (1972) Soft, stiff and servo-controlled testing machines: a review with reference to rock failure. *Eng Geol* 6(3):155–189
- Ingraffea AR, Gunsallus KL, Beech JF, Nelson PP (1984) A short-rod based system for fracture toughness testing of rock. In: Chevron-notched specimens: testing and stress analysis, ASTM International
- Jin Z, Li W, Jin C, Hambleton J, Cusatis G (2018) Anisotropic elastic, strength, and fracture properties of Marcellus shale. *Int J Rock Mech Min Sci* 109:124–137
- Kabir P, Ulm FJ, Akono AT (2017) Rate-independent fracture toughness of gray and black kerogen-rich shales. *Acta Geotech* 12:1–21
- Kataoka M, Obara Y (2015) Size effect in fracture toughness of sandstone. In: 13th ISRM international congress of rock mechanics, international society for rock mechanics
- Khan K, Al-Shayea N (2000) Effect of specimen geometry and testing method on mixed mode I–II fracture toughness of a limestone rock from Saudi Arabia. *Rock Mech Rock Eng* 33(3):179–206
- Kim KT, Baant ZP, Yu Q (2013) Non-uniqueness of cohesive-crack stress-separation law of human and bovine bones and remedy by size effect tests. *Int J Fract* 181(1):67–81
- Laubie H, Ulm FJ (2014a) Irwin's conjecture: crack shape adaptability in transversely isotropic solids. *J Mech Phys Solids* 68:1–13
- Laubie H, Ulm FJ (2014b) Plane-strain crack problem in transversely isotropic solids for hydraulic fracturing applications. *J Eng Mech* 140(12):04014,092
- Lee HP, Olson JE, Holder J, Gale JF, Myers RD (2015) The interaction of propagating opening mode fractures with preexisting discontinuities in shale. *J Geophys Res Solid Earth* 120(1):169–181
- Li W, Jin C, Cusatis G (2016) Integrated experimental and computational characterization of shale at multiple length scales. In: *New frontiers in oil and gas exploration*, Springer, pp 389–434
- Li W, Rezakhani R, Jin C, Zhou X, Cusatis G (2017) A multiscale framework for the simulation of the anisotropic mechanical behavior of shale. *Int J Numer Anal Methods Geomech* 41(14):1494–1522
- Li C, Chau VT, Xie H, Baant ZP (2018a) Recent advances in mechanics of fracking and new results on 2D simulation of crack branching in anisotropic gas or oil shale. *Acta Mech* 229:1–18
- Li W, Zhou X, Carey JW, Frash LP, Cusatis G (2018b) Multiphysics lattice discrete particle modeling (M-LDPM) for the simulation of shale fracture permeability. [arXiv:1803.09831](https://arxiv.org/abs/1803.09831)
- Lim I, Johnston I, Choi S, Boland J (1994) Fracture testing of a soft rock with semi-circular specimens under three-point bending. Part 1-mode I. *Int J Rock Mech Min Sci Geomech Abstr* 31(3):185–197
- Mefford CH, Qiao Y, Salviato M (2017) Failure behavior and scaling of graphene nanocomposites. *Compos Struct* 176:961–972
- Salviato M, Chau VT, Li W, Baant ZP, Cusatis G (2016a) Direct testing of gradual postpeak softening of fracture specimens of fiber composites stabilized by enhanced grip stiffness and mass. *J Appl Mech* 83(11):111,003
- Salviato M, Kirane K, Ashari SE, Baant ZP, Cusatis G (2016b) Experimental and numerical investigation of intra-laminar energy dissipation and size effect in two-dimensional textile composites. *Compos Sci Technol* 135:67–75
- Schmidt R (1977) Fracture mechanics of oil shale-unconfined fracture toughness, stress corrosion cracking, and tension test results. In: *The 18th US Symposium on Rock Mechanics (USRMS)*, American Rock Mechanics Association
- Sierra R, Tran M, Abousleiman Y, Slatt R (2010) Woodford shale mechanical properties and the impacts of lithofacies. In: *44th US rock mechanics symposium and 5th US-Canada rock mechanics symposium*, American Rock Mechanics Association
- Sih GC, Paris P, Irwin GR (1965) On cracks in rectilinearly anisotropic bodies. *Int J FractMech* 1(3):189–203
- Tang T, Baant ZP, Yang S, Zollinger D (1996) Variable-notch one-size test method for fracture energy and process zone length. *Eng Fract Mech* 55(3):383–404
- Wang Y, Hu X (2017) Determination of tensile strength and fracture toughness of granite using notched three-point-bend samples. *Rock Mech Rock Eng* 50(1):17–28
- Wang H, Zhao F, Huang Z, Yao Y, Yuan G (2017) Experimental study of mode-I fracture toughness for layered shale based on two ISRM-suggested methods. *Rock Mech Rock Eng* 50(7):1933–1939
- Wendner R, Vorel J, Smith J, Hoover CG, Baant ZP, Cusatis G (2015) Characterization of concrete failure behavior: a comprehensive experimental database for the calibration and validation of concrete models. *Mater Struct* 48(11):3603–3626
- Yan W, Chen J, Deng J, Zhou Y, Wang K (2017) Experimental study of the mode-I fracture toughness on sichuan basin gas shale under air dried and water saturated conditions. In: *51st US rock mechanics/geomechanics symposium*, American Rock Mechanics Association
- Zeng X, Wei Y (2017) Crack deflection in brittle media with heterogeneous interfaces and its application in shale fracking. *J Mech Phys Solids* 101:235–249
- Zeng QD, Yao J, Shao J (2018) Numerical study of hydraulic fracture propagation accounting for rock anisotropy. *J Petrol Sci Eng* 160:422–432
- Zia H, Lecampion B, Zhang W (2018) Impact of the anisotropy of fracture toughness on the propagation of planar 3D hydraulic fracture. *Int J Fract* 211:1–21

**Publisher's Note** Springer Nature remains neutral with regard to jurisdictional claims in published maps and institutional affiliations.